Available online at www.sciencedirect.com
SCIENCE DIRECT
International Journal of Heat and Mass Transfer 49 (2006) 3717–3727
International Journal of HEAT and MASS TRANSFER
www.elsevier.com/locate/ijhmt

Experimental and numerical study of downward bubbly flow in a pipe

O.N. Kashinsky, P.D. Lobanov, M.A. Pakhomov, V.V. Randin, V.I. Terekhov *

Kutateladze Institute of Thermophysics SB RAS, 1, Acad. Lavrent'ev Avenue, 630090 Novosibirsk, Russia

Available online 6 June 2006

Abstract

An experimental and numerical study of the local structure of downward gas–liquid flow in a vertical pipe with 20-mm inner diameter is reported. In the experiment, the electrodiffusion technique was used in combination with electrical conductivity measurements. To examine the effect of gas-phase dispersion on flow characteristics, two different gas–liquid mixers were used capable of producing large-diameter (>1 mm) and small-diameter (<1 mm) gas bubbles at identical rate characteristics of the flow. The unified heterogeneous-medium mechanics approach was used to develop, in the Eulerian two-velocity approximation, a calculation model for downward turbulent liquid/air bubble flows. It is shown that, as the volumetric gas flow rate of the mixture at the inlet to the pipe increases, local maxima of continuous phase velocity and bubble concentration emerge in the near-wall zone of the flow, with liquid turbulence suppressed in the wall zone and enhanced in the core of the flow.

1. Introduction

Turbulent gas–liquid flows are widely used in various technological applications such as nuclear power engineering, heat power engineering, chemical apparatus, food industry, and pharmaceutical industry. Information about the structure and average and fluctuational characteristics of bubbly flows is necessary in design of advanced technological equipment.

A good deal of papers was devoted to the experimental and numerical modeling of vertical bubbly flows [1–25]. Presently, there is a broad range of publications in which the case of upward flows, that were studied most extensively, was addressed [11,13–23]. Downward flows were investigated more scantily [1–13,16,25]. The first works on downward gas–liquid flows were reported in [1–3]. In [1], the void fraction and pressure drop in upward and downward flows were measured. It was shown that, with volumetric gas flow rate ratio at the inlet to the pipe being identical, the actual void fraction of downward flow is normally higher than that of upward flow. In [2], the void fraction, the hydraulic resistance, and the heat transfer and structure of downward bubbly flows in the co-current and gas-phase choking regime, were examined. The local void fraction distribution was shown to display a maximum located some distance away from the pipe wall, with a higher gradient of this quantity in the near-wall region, where it decreases to zero, and with a plateau in the core of the flow. The distribution of liquid velocity also exhibits a maximum in the near-wall region.

The authors of [3] investigated the local structure of downward bubbly flow with small bubbles in a vertical pipe with 15-mm inner diameter. The local void fraction was shown to display a peak in the near-wall region. A notable decrease in the fluctuation velocity of liquid in the near-wall zone and substantial reduction of the wall-friction pulsation intensity compared to the case of single-phase flow were observed. Simultaneously, in the central region the fluctuation velocity was higher than in the case of single-phase flow. The authors of [4] examined the turbulent structure and the distribution of phases in downward bubbly flow in a pipe with 57.2-mm inner diameter. In this study, the local void fraction, the profiles of liquid velocity, and the Reynolds stresses were measured. The authors of [5] studied a downward flow in pipes with inner diameters 16 and 24 mm.

* Corresponding author. Tel.: +7 383 3306736; fax: +7 383 3308480.
E-mail addresses: kashinsky@itp.nsc.ru (O.N. Kashinsky), lobanov@itp.nsc.ru (P.D. Lobanov), pakhomov@ngs.ru (M.A. Pakhomov), randin@itp.nsc.ru (V.V. Randin), terekhov@itp.nsc.ru (V.I. Terekhov).

0017-9310/$ - see front matter © 2006 Elsevier Ltd. All rights reserved.
doi:10.1016/j.ijheatmasstransfer.2006.02.004

Nomenclature

C^{D} drag coefficient
C_{L} coefficient in the lift force
D_{xL}, D_{rL} turbulent diffusivities of drops in the axial and radial directions due to the stochastic motion of drops and their entrainment into the gas flow by intense vortices (m^2/s)
d bubble diameter (m)
g gravitational acceleration (m/s^2)
k turbulent kinetic energy (m^2/s^2)
P pressure (N/m^2)
R tube radius (m)
U, V velocity component in axial and radial directions (m/s)
$\langle uv\rangle = -v_T \frac{\partial U}{\partial r}$ turbulent stresses in gas-phase (m^2/s^2)
$\langle u_P v_P\rangle$ turbulent stresses in dispersed phase (m^2/s^2)
$U^R = U - U_b$ relative velocity of the two phases (m/s)
$\langle u^2\rangle$, $\langle v^2\rangle$ rms velocity fluctuations in axial and radial directions (m^2/s^2)
U_* wall friction velocity (m/s)
U_l superficial liquid velocity
x, r axial and radial coordinates (m)
y coordinate normal to the wall (m)
y_b the distance from wall to the bubble center (m)
$y_\lambda = y/\sqrt{vk/\tilde{\varepsilon}}$ Taylor microscale
$\Re$ absolute gas constant (J/(mol K))
$Re = U_1 2R/v$ Reynolds number
$Re_b = d\sqrt{(U-U_b)^2 + (V-V_b)^2}/v$ Reynolds number of disperse phase
$Re_T = k^2/\varepsilon v$ turbulent Reynolds number
$Tu = \sqrt{1/3(\langle u^2\rangle + \langle v^2\rangle + \langle w^2\rangle)}/U$ turbulent intensity in the liquid flow

Greek symbols
α local void fraction
β volumetric gas flow rate ratio
$\varepsilon = \tilde{\varepsilon} + \hat{\varepsilon}$ dissipation rate (m^2/s^3)
$\tilde{\varepsilon}$ dissipation rate (m^2/s^3)
$\hat{\varepsilon} = 2\mu/\rho[\partial(\sqrt{k})/\partial r]^2$ rate of energy dissipation in the near-wall zone ($y_+ \leqslant 15$) (m^2/s^3)
$\Gamma^E = v_T/\langle u^2\rangle$ is the geometric scale of the continuous phase turbulence (m)
μ dynamic viscosity ((N s)/m^2)
v kinematic viscosity (m^2/s)
$\Omega^\varepsilon = (15v/\varepsilon)^{1/2}$ time microscale (s)
Ω^E Eulerian time macroscale (s)
Ω^L Lagrangian time macroscale (s)
$\Omega^{\varepsilon L}$ time of particle interaction with the intense vortices (s)
ρ density (kg/m^3)
$\tau = \frac{4}{3}\frac{\rho_b d^2}{\rho v Re_b C_D}$ particle relaxation time (s)

Subscripts
1 inlet parameter
b bubble
i current calculation cross-section along the axial direction
$i-1$ previous calculation cross-section along the axial direction
T turbulent parameter
W parameter at the wall
$+$ denotes the dimensionless variables in dynamic universal units

In recent years, studies of downward bubbly flows became more and more intense [6–13,15,16,24]. In [6,7,12], the electrodiffusion technique was used to measure the wall friction, the void fraction profiles, the axial velocity of liquid, and the fluctuation component of this velocity. The authors of [6,7] examined the turbulent structure and local characteristics of downward flow in a vertical pipe with 42.2-mm inner diameter. The measurements were performed for two diameters of gas bubbles, 0.8 and 1.47 mm. In these studies, particular attention was given to measurements in the near-wall zone of the flow. An increase in the friction compared to the case of single-phase flow was established. Suppression of friction pulsations in the near-wall zone of the flow was observed. Kashinsky et al. [12] examined the local structure of downward flow in a pipe with 20-mm inner diameter at low integral volumetric gas flow rate ratio ($\beta \leqslant 3\%$). It was found that the gas-phase introduced into the flow suppresses the fluctuations of the liquid velocity in the near-wall zone.

In [8], downward bubbly flows in pipes with inner diameters 25.4 and 50.8 mm were investigated. The pipe length was 3.81 m. The measurements were performed at three sections along the pipe. In this work, the influence of the relative motion of the phases on the liquid velocity, local void fraction, and bubble sizes was examined. In [9–11], laser Doppler anemometry (LDA) was employed to measure the profiles of void fraction, average velocities of the gas and liquid phases, and longitudinal velocity of the liquid phase. A combined technique based on the conduction method and on the film-anemometer technique was used to measure the radial profiles of bubble velocity and gas void fraction profiles. It was noted that bubbles present in the downward flow result in the formation of a plateau in the distributions of liquid velocity. Displacement of the maximum velocity of liquid off the channel axis was reported. Apart from the reported experimental study, Hibiki et al. [9] proposed a classification of downward bubbly flows considering the position of the void fraction peak

in the pipe: (1) core-peaked, (2) bell-typed, (3) off-center peaked. In addition, the authors proposed an improved one-dimensional drift-flux model for downward flow [24,25]. A simple correlation for predicting the local void fraction of downward flow was proposed. To construct the model, it is necessary to know the point at which the bubble concentration vanishes in the flow. These data can be obtained only from experiments, which circumstance makes the developed model less valuable.

Experiments showed the absence of bubbles in the near-wall zone of downward flow. Simultaneously, it was found that even low volumetric gas flow rate ratios ($\beta < 5\%$) may have a profound effect on the profiles of average and pulsating characteristics of the liquid phase.

Among the whole variety of numerical simulation studies of bubbly flows, the works [13–15,17–24] deserve mention. For the most part, these studies addressed the case of upward flow of two-phase gas–liquid systems. Some results for downward gas–liquid flows were only reported in [13,15].

A numerical model predicting how the shape of void fraction profiles affects the distribution of temperature and liquid-phase velocity in vertical flows was developed in [13]. This model can be applied both to upward and downward flows. In this work, enhanced turbulence due to gas bubbles present in the flow was taken into account. The turbulent viscosity was represented as a linear combination of two terms, one term being due to the liquid-phase turbulence, which can be calculated by the Reichardt formula, and the other term modeling the additional viscosity due to the relative gas motion. The second term involves some empirical constants, this circumstance making the developed numerical model less general.

In [15], a diffusion-inertia model for the transport of low-inertia particles of arbitrary density was proposed. The predicted data were compared with the experimental data of [16] for gas–liquid flows in vertical pipes (the cases of downward and upward flow under various conditions of the effect due to the gravity force). It was shown possible, in principle, to analyze bubbly flows with the help of the diffusion-inertia model, initially developed for gas-dispersed flows. To calculate the liquid turbulence, the k–ε model of turbulence for single-phase flow was used.

Antal et al. [18] developed a numerical model for transport phenomena in laminar upward bubbly flow. The model was based on the Eulerian two-velocity approach. The major forces acting on bubbles in the laminar flow were the lifting (Saffman) force and the wall force. In [19], a numerical and experimental study of turbulent bubbly flow in a triangular channel was reported. In [21,23], the case of polydispersed two-phase flows was addressed. The model makes it possible to allow for the shift of the bubble concentration maximum from the near-wall zone towards the flow core observed when the dispersed-phase size increases above some critical value. Troshko and Hassan [22] developed a numerical model involving the law of the wall for vertical mono-dispersed bubbly flow in a pipe.

In [17,19,21–23], to predict the liquid-phase turbulence, a two-equation model of turbulence extended to the case of two-phase flow, was used.

It can be stated that, in spite of the intensive recent efforts aimed at numerical investigation of downward gas–liquid flows, gained data cover only a narrow range of parameters and therefore apply only to particular conditions.

The purpose of the present study was a numerical and experimental investigation of the structure of downward gas–liquid flow in a pipe. A model constructed around the Eulerian representation for both phases was developed to numerically examine the structure of downward mono-dispersed gas–liquid flow. The influence of bubble sizes on local flow quantities was evaluated.

2. Experimental setup

The experimental setup was a two-phase flow loop, closed for the liquid flow and open for the gas flow (see Fig. 1). The liquid from a storage tank, pushed by

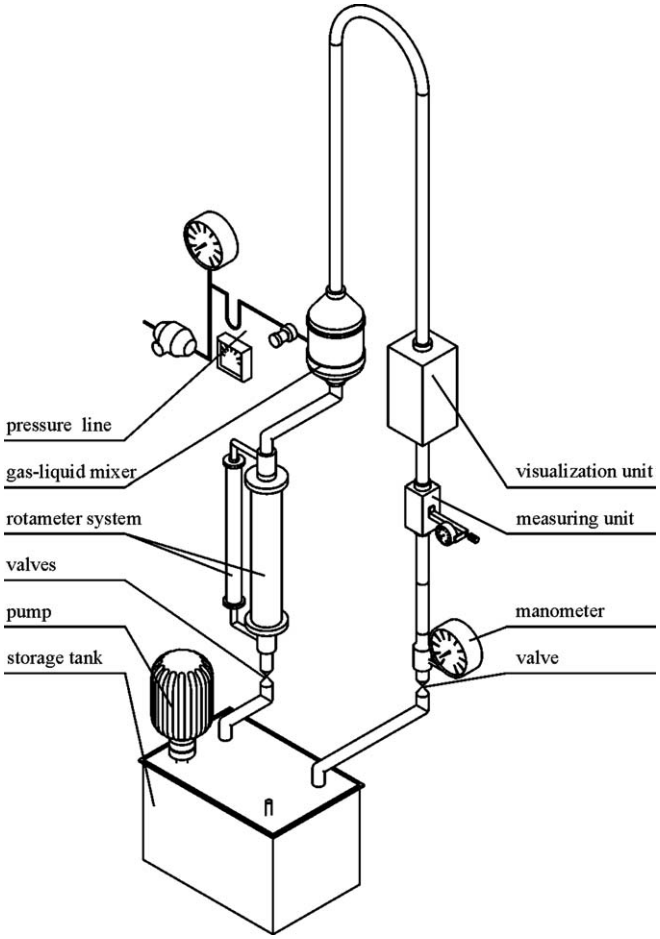

Fig. 1. Experimental setup.

centrifugal pump, entered, through a rotameter system, a gas–liquid mixer. The rate of the liquid flow could be adjusted by valves. The gas was supplied to the mixer from high-pressure pipeline. The gas pressure, dropped down with the help of a pressure regulator installed at the inlet to the setup, was 1 atm. The gas–liquid flow was produced in an upward section to enter, through a *U*-bend, a downward section, presenting a vertical stainless-steel pipe with inner diameter $2R = 20$ mm. At this section, visualization unit and measuring unit were mounted. From the outlet of the downward section, the gas–liquid mixture entered the storage tank, in which gas separation was organized. In the bottom part of the test section, manometer and valve, used to maintain the test-section pressure in excess of the atmospheric pressure and to avoid cavitation and gas leakages from outside, were installed. The temperature of the test liquid was kept constant within 25 ± 0.2 °C by an automated temperature control system.

The local flow quantities were measured 2 m ($x/(2R) = 100$) downstream of the inlet to the downward section of the pipe. The superficial velocity of the liquid varied in the interval $U = 0.3$–0.5 m/s, and the volumetric gas flow rate ratio was $\beta = 0$–0.1.

The hydrodynamic characteristics of the flow were measured using the electrochemical technique. The test liquid was a solution of 0.005 M potassium ferro- and ferricyanide and 0.25 M of sodium carbonate in distilled water.

To determine the profiles of liquid velocity and the local void fraction profiles, a "blunt-nose" type flow velocity probe was used. The same probe was simultaneously operated in the electroconductivity mode [26,27]. The sensor was a 50 μm-diameter platinum wire welded into a conical glass capillary. The diameter of the working tip of the sensor was 60 μm. The glass capillary was cemented into a holder mounted on a traversing mechanism that permitted accurate positioning of the velocity probe across the channel.

To measure the wall friction, an electrochemical wall shear stress probe was used. The probe was a platinum plate, cemented into the pipe wall and grounded flush with it.

To generate bubbly flow, two gas–liquid mixers were used. In the first mixer, the gas was injected into the gas flow through 12 capillaries with inner diameter 0.2 mm installed in the settling chamber, whose inner diameter was 116 mm. The velocity of liquid in the settling chamber was low, and free departure of bubbles from capillaries could be assumed. This mixer was used to produce large bubbles with a mean diameter of 1.5–2 mm.

To generate smaller bubbles, another mixer was used. The liquid flow from the pump was divided into two flows feeding two pipe lines equipped with individual valves and rotameters. The capillaries were cemented into a glass insert with inner diameter 20 mm, and the butt ends of the capillaries were grounded flush with the wall of the insert. Bubbles were generated in the annular gap formed by the inner surface of the insert and the outer surface of the central body, installed co-axially with the insert. The width of the annular gap was 0.5 mm. By changing the rate of the liquid flow through the annular gap, the size of produced bubbles in one and the same regime could be varied. This mixture was used to produce small-diameter bubbles, whose mean diameter ranged in the interval 0.4–0.9 mm.

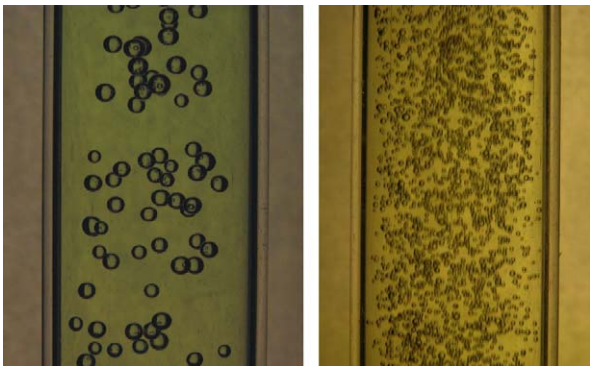

Fig. 2. Photos of bubbles from different mixers.

The bubble sizes were determined by filming the flow with a Nikon Coolpix 5700 digital camera. The filming was done in a special optical section, where the glass tube was placed in a Plexiglas box filled with an immersion liquid for avoiding optical distortions. The photographs of generated bubbles were processed on a computer using special software. Fig. 2 shows photographs of the flow taken at identical rate parameters (superficial gas- and liquid-flow velocities), but at different bubble sizes.

A detailed analysis of measurement uncertainties for the electrodiffusional technique applied was reported elsewhere [26,27]. The measurement uncertainty for the velocity of liquid and for the fluctuations of this velocity was 4% and 15%, respectively. The uncertainty in the determination of mean bubble sizes was about 5%.

3. Statement of the problem

On the whole, the mathematical model used in the present study is the same as in [28,29]. The system of governing equations is based on the Euler two-fluid approach, previously approbated by the authors for two-phase flows with liquid droplets and phase changes. In [28,29], turbulent gas-droplets flow in a pipe [28] and turbulent wall gas-droplet jet flow [29] with phase changes were simulated, and a comparison with experimental data was performed. The comparison with the experiment for the case of the pipe flow showed the predicted data to well agree with experimental data both in terms of average and turbulent characteristics; the latter gave us grounds to employ the model of [28,29] for the numerical analysis of dynamic characteristics of bubbly flows in vertical channels.

A substantial advantage of the two-fluid model compared to the trajectory Lagrangian method is that, in this model, equations of one and the same type and, hence, a unified numerical solution algorithm for these equations,

are used to predict the transport phenomena in both phases [30–32]. The two-fluid models allow one to accurately describe the forces acting on bubbles in a gas–liquid flow and responsible for radial displacement of the dispersed phase.

The main difference of the present study from [28,29] consists in that, here, we simulate turbulent isothermal liquid-phase/gas-bubble flow with regard for the interaction between the phases, the stochastic motion of the bubbles, and the turbophoresis. Like in the majority of previous numerical simulations of bubbly flows [13,15,21–23], in the present study we ignore fractionation and coagulation of bubbles. The interaction of bubbles with the channel wall is ignored either because, according to the experimental data of [6,7,12], in downward flows in the near-wall zone of the channel there exists a region free of bubbles. The flow was assumed isothermal, with no phase transitions occurring at the bubble/liquid interface.

4. Governing equations

4.1. System of equations for the liquid phase

With the adopted assumptions, the set of the continuity equation, the equation of motion in the axial direction, and the equation of state for an axisymmetric two-phase heterogeneous flow in the boundary-layer approximation is

$$\begin{aligned}
&\frac{\partial U}{\partial x}+\frac{1}{r}\frac{\partial (rV)}{\partial r}=0,\\
&\rho\left[U\frac{\partial U}{\partial x}+\frac{V}{r}\frac{\partial (rU)}{\partial r}\right]=-\frac{\partial P}{\partial x}+\frac{1}{r}\frac{\partial}{\partial r}\left[r(\mu+\mu_{\mathrm{T}})\frac{\partial U}{\partial r}\right]\\
&\qquad\qquad -\frac{3C^{D}\rho\alpha}{4d(1-\alpha)}U^{\mathrm{R}}|\vec{U}^{\mathrm{R}}|,\\
&\rho=(1-\alpha)P/(\Re T);\quad \partial P/\partial r=0.
\end{aligned}\tag{1}$$

The equation of motion of the liquid phase involves an additional term that takes into account the dynamic interaction between the phases.

In (1), $\vec{U}^{\mathrm{R}}=\vec{U}-\vec{U}_{\mathrm{b}}$, and C^{D} is the drag coefficient for the bubbles:

$$C^{D}=\begin{cases}48/Re_{\mathrm{b}}, & Re_{\mathrm{b}}<96,\\ 0.5, & Re_{\mathrm{b}}\geqslant 96.\end{cases}$$

4.2. System of equations for the dispersed phase (bubbles)

In the present study, the following forces acting on a bubble in a turbulent flow are considered: the drag, the gravity force, the turbophoresis force, the Archimedean force, the lift (Saffman) force due to the shear in the liquid phase velocity, and the effect due to the associated mass.

In the cylindrical coordinate system, the system of the continuity equation and the equation for the average velocity components of axisymmetric dispersed flow in the axial direction can be written as follows:

$$\begin{aligned}
&\frac{\partial(\alpha U_{\mathrm{b}})}{\partial x}+\frac{1}{r}\frac{\partial(r\alpha V_{\mathrm{b}})}{\partial r}=0,\\
&\underbrace{U_{\mathrm{b}}\frac{\partial(\alpha U_{\mathrm{b}})}{\partial x}+\frac{V_{\mathrm{b}}}{r}\frac{\partial(r\alpha U_{\mathrm{b}})}{\partial r}}_{\mathrm{I}}+\underbrace{\frac{\partial(\alpha\langle u_{\mathrm{b}}^{2}\rangle)}{\partial x}}_{\mathrm{II}}+\underbrace{\frac{1}{r\beta}\frac{\partial}{\partial r}[r\beta\langle u_{\mathrm{P}}v_{\mathrm{P}}\rangle]}_{\mathrm{III}}\\
&\quad=\pm g\left[\underbrace{\frac{(1-\rho/\rho_{\mathrm{b}})}{(1+0.5\rho/\rho_{\mathrm{b}})}+\alpha}_{\mathrm{IV}}\right]-\underbrace{\frac{3C^{D}\alpha}{4d}U^{\mathrm{R}}|\vec{U}^{\mathrm{R}}|}_{\mathrm{V}}-\underbrace{\frac{D_{\mathrm{xb}}}{\tau}\frac{\partial(\ln\alpha)}{\partial r}}_{\mathrm{VI}}.
\end{aligned}\tag{2}$$

Here, I is the momentum convection, II is the turbophoresis force, III is the turbulent stress in the dispersed phase, IV is the effect due to the associated mass and Archimedean force, V is the drag, and VI is the diffusion displacement of bubbles due to their concentration gradient. The force due to the associated mass (IV) in (2) is written in the form that was validated for a particle migrating in an inviscid liquid flow [33] and was used in the majority of simulation studies where the motion of particles or bubbles in turbulent flows was treated.

The equation of bubble motion in the radial direction is

$$\begin{aligned}
&\underbrace{U_{\mathrm{b}}\frac{\partial(\alpha V_{\mathrm{b}})}{\partial x}+\frac{V_{\mathrm{b}}}{r}\frac{\partial(r\alpha V_{\mathrm{b}})}{\partial r}}_{\mathrm{I}}+\underbrace{\frac{\partial(\alpha\langle v_{\mathrm{b}}^{2}\rangle)}{\partial r}}_{\mathrm{II}}\\
&\quad=\underbrace{\frac{3v_{\mathrm{T}}C^{D}}{4d}|U^{\mathrm{R}}|\frac{\partial\alpha}{\partial r}}_{\mathrm{III}}+\underbrace{C_{\mathrm{L}}\alpha U^{\mathrm{R}}|\frac{\partial U}{\partial r}|}_{\mathrm{IV}}-\underbrace{\frac{3C_{\mathrm{D}}\alpha}{4d}(U^{\mathrm{R}})|\vec{U}^{\mathrm{R}}|}_{\mathrm{V}}\\
&\quad\quad-\underbrace{\left(C_{\mathrm{W1}}-C_{\mathrm{W2}}\frac{d_{\mathrm{b}}}{2y_{\mathrm{b}}}\right)\frac{4\alpha|U^{\mathrm{R}}|^{2}}{d}}_{\mathrm{VI}}-\underbrace{\frac{D_{\mathrm{rb}}}{\tau}\frac{\partial\ln\alpha}{\partial r}}_{\mathrm{VII}}.
\end{aligned}\tag{3}$$

The radial displacement of bubbles is due to the following forces: I—momentum convection, II—turbophoresis force, III—turbulent dispersion [23], IV—lift (Saffman) force, V—drag, VI—wall force, and VII—diffusion displacement of bubbles due to their concentration gradient. The brackets denote averaging over the ensemble of turbulent realizations.

Here $\langle u_{\mathrm{P}}v_{\mathrm{P}}\rangle$ is the turbulent stresses in the dispersed phase [34], D_{xb} and D_{rb} are the coefficients of the turbulent diffusion of bubbles in the axial and radial directions due to the chaotic migration of particles and their involvement in the gas flow by the high-energy eddies [34], and C_{L} is the coefficient of proportionality in the expression for the lift (Saffman) force (IV). The latter coefficient can be determined from the data of [20]. It should be noted that in the expression given in [20] the coefficient C_{L} changes its sign as the bubble diameter increases over 5.6 mm.

The wall force (VI) retains its direction towards the channel axis both for upward and downward flows. As a bubble approaches the channel wall, the flow pattern around the bubble undergoes substantial changes. With regard for the condition of no-slip of liquid at the rigid pipe surface, the velocity of the liquid flow past a bubble on the

side of the bubble facing the wall is lower than on the opposite side. As a result, there arises a hydrodynamic force pushing the bubble from the wall toward the channel axis. According to Antal et al. [18],

$$\left(C_{W1} - C_{W2}\frac{d}{2y_b}\right)\frac{2\alpha\rho|U^R|^2}{d} = 0 \quad \text{if } y_b > \frac{C_{W2}}{2C_{W1}}d,$$

where $C_{W1} = -0.06U^R - 0.104$ and $C_{W2} = 0.147$.

4.3. Two-equation model of liquid-phase turbulence

The equations for the turbulence energy k and for the rate of its dissipation $\tilde{\varepsilon}$ modified to the case of a dispersed phase present in the flow have the form

$$\rho\left[U\frac{\partial k}{\partial x} + \frac{V}{r}\frac{\partial(rk)}{\partial r}\right] = \frac{\rho}{r}\frac{\partial}{\partial r}\left[r\left(\mu + \frac{\mu_T}{\sigma_k}\right)\frac{\partial k}{\partial r}\right] + \Pi - \rho\varepsilon + \Pi_k + C_p\frac{\alpha|\vec{U}^R|^3}{d(1-\alpha)} \tag{4}$$

$$\rho\left[U\frac{\partial\tilde{\varepsilon}}{\partial x} + \frac{V}{r}\frac{\partial(r\tilde{\varepsilon})}{\partial r}\right] = \frac{\rho}{r}\frac{\partial}{\partial r}\left[r\left(\mu + \frac{\mu_T}{\sigma_\varepsilon}\right)\frac{\partial\tilde{\varepsilon}}{\partial r}\right] + \frac{\tilde{\varepsilon}}{k}(C_{\varepsilon 1}f_1\Pi - C_{\varepsilon 2}\tilde{\varepsilon}\rho f_2) + \frac{C_{\varepsilon 3}}{4}\frac{k^2}{\tilde{\varepsilon}}\frac{\partial U}{\partial x}\left(\frac{V}{r}\right)^2 + \Pi_\varepsilon + \frac{\tilde{\varepsilon}}{k}C_p\frac{\alpha|\vec{U}^R|^3}{d(1-\alpha)}. \tag{5}$$

The constants and the damping functions are the same as in the Hwang and Lin model of turbulence for single-phase flow [35]. In (5), $\Pi = \mu_T\left(\frac{\partial U}{\partial r}\right)^2$ is the production of the turbulence energy from the average motion, $\Pi_k = -\frac{\mu}{2}\frac{\partial}{\partial r}\left(\frac{k}{\varepsilon}\frac{\partial\hat{\varepsilon}}{\partial r}\right)$, $\Pi_\varepsilon = -\frac{\mu}{r}\frac{\partial}{\partial r}\left(r\frac{\varepsilon}{k}\frac{\partial k}{\partial r}\right)$, and $\hat{\varepsilon} = 2\mu/\rho[\partial(\sqrt{k})/\partial r]^2$ is the rate of energy dissipation in the near-wall zone ($y_+ \leqslant 15$); for $y_+ > 15$, $\hat{\varepsilon} = 0$.

The third term in the right-hand side of (5) accounts for the stretching of turbulent eddies; in the case of internal flow, $C_{\varepsilon 3} = 0.79$. The last term in (5), whose form was borrowed from [21], takes into account the bubble-induced generation of turbulent energy. In the present study, for the downward flow the value $C_P = 0.95$ was adopted.

4.4. Equations for the second momentums of dispersed-phase velocity fluctuations

The second momentums of the turbulent fluctuations of bubble velocity in the longitudinal and cross-flow directions can be found from the equation [34]

$$\underbrace{U_b\frac{\partial\langle u_b^2\rangle}{\partial x} + \frac{V_b}{r}\frac{\partial(r\langle u_b^2\rangle)}{\partial r}}_{\text{I}} + \underbrace{\frac{1}{r\beta}\frac{\partial}{\partial r}\left[\frac{\partial(r\beta\langle u_L^2 v_L\rangle)}{\partial r}\right]}_{\text{II}} + \underbrace{2\langle u_b^2\rangle\frac{\partial U_b}{\partial x}}_{\text{III}} = \underbrace{\frac{2}{\tau}\left(q_P\langle u^2\rangle - \langle u_b^2\rangle\right)}_{\text{IV}} \underbrace{U_b\frac{\partial\langle v_b^2\rangle}{\partial x} + \frac{V_b}{r}\frac{\partial(r\langle v_b^2\rangle)}{\partial r}}_{\text{I}} + \underbrace{\frac{1}{r\beta}\frac{\partial}{\partial r}\left[\frac{\partial(r\beta\langle v_b^3\rangle)}{\partial r}\right]}_{\text{II}} = \underbrace{\frac{2}{\tau}\left(q_P\langle v^2\rangle - \langle v_b^2\rangle\right)}_{\text{IV}}. \tag{6}$$

The terms in the right-hand sides of (6) are sources of bubble velocity fluctuations in the local-equilibrium approximation, which allows for the participation of the dispersed phase in the high-energy fluctuations of the liquid phase only. It is seen from (6) that the intensity of the chaotic migration of contamination in the axial direction increases not only due to the convection (I) and diffusion (II) transport of the impurity, and due to the action of the viscosity force (IV), but also due to the turbulence generation from the average motion of bubbles (III). The third momentums of velocity pulsations give the diffusion flux of energy due to the chaotic motion of bubbles in the axial and radial directions [34]:

$$\langle u_P^2 v_P\rangle = -\frac{\tau\langle v_b^2\rangle}{3}\frac{\partial\langle u_b^2\rangle}{\partial r}; \quad \langle v_b^3\rangle = -\tau\langle v_b^2\rangle\frac{\partial\langle v_b^2\rangle}{\partial r}. \tag{7}$$

The transfer of the energy related with the chaotic motion of bubbles is defined by the intensity of dispersed-phase velocity fluctuations in the radial direction and by the gradient of corresponding second momentums.

5. Boundary conditions

At the pipe axis, the symmetry conditions for the gas- and liquid-phase flows were set:

$$\frac{\partial U}{\partial r} = V = \frac{\partial U_b}{\partial r} = V_b = \frac{\partial\langle u_b^2\rangle}{\partial r} = \frac{\partial\langle v_b^2\rangle}{\partial r} = \frac{\partial k}{\partial r} = \frac{\partial\tilde{\varepsilon}}{\partial r} = 0.$$

At the wall, for the velocity of liquid the no-slip condition and the impermeability condition hold, and the gas kinetic energy and the dissipation rate of this energy are zero:

$$U = V = 0; \quad k = \tilde{\varepsilon} = 0.$$

The average axial and radial velocities of bubbles, and the pulsations of these velocities are also zero:

$$U_b = V_b = \frac{\partial\langle u_b^2\rangle}{\partial r} = \frac{\partial\langle v_b^2\rangle}{\partial r} = 0.$$

At the inlet section of the pipe, all characteristics are distributed uniformly:

$$U = U_1, \quad V = V_1, \quad \beta = \beta_1, \quad d = d_1, \quad k = k_1, \quad \tilde{\varepsilon} = \tilde{\varepsilon}_1.$$

The initial profiles for k and $\tilde{\varepsilon}$ are given in [36]. In the present study, the inlet liquid-phase turbulence number was adopted to be $Tu_1 = 4\%$.

6. Numerical algorithm

To solve the parabolic equations (the equation of liquid motion, the equation of the two-parametric model of turbulence, the equation for the axial velocity of bubbles, and the pulsational equations for the dispersed phase), we used the method previously developed for boundary-layer flows in [37]. The difference scheme is accurate to the second order along both directions. To solve the system, the sweep method was used [38]. The hyperbolic

equations (the continuity equations for the liquid and bubbles, and the equation for the radial velocity of the dispersed phase) were solved using the Keller box method described in [38]. The Keller box method has the second order of accuracy along both coordinates.

The calculations in the present study were performed on a computation grid having a total of 200 nodes in both (axial and radial) directions. Methodical calculations were also performed on a nested grid with 300 nodes over the pipe length and 300 nodes over the pipe radius. Further increase in the number of calculation nodes caused no substantial changes in the calculated data. The calculation node nearest to the wall was located at $y_+ = 1$. To more accurately calculate the turbulent parameters in the near-wall zone with large gradients of these parameters, we used a grid logarithmically densening in the radial direction. The densening constant was chosen so that at least ten nodes were available in the viscous sublayer. Since the grid was non-uniform in the transverse (cross-flow) direction, we could conveniently transform the coordinate r so that to solve the equations on a uniform grid in the computation domain. In the present study, we used the transformation of coordinates given in [38]. In the axial direction, the grid was uniform.

7. Experimental and calculation data, and their discussion

The size of the dispersed phase was $d = 0.61$–0.73 and 1.62–1.8 mm; this size was constant both over the pipe length and across the pipe. All computations were performed for mono-disperse composition of the two-phase flow. The inlet gas flow rate ratio was $\beta = 1$–10%. The range of superficial liquid velocity was $U_1 = 0.3$–0.5 m/s, corresponding to the pipe Reynolds number $Re = U_1 2R/\nu \approx 6200$–$10^4$.

7.1. Longitudinal velocities of the phases

Cross-sectional profiles of the velocities of the phases for various sizes of the dispersed phase are shown in Fig. 3a and b ($U_1 = 0.3$ and $U_1 = 0.4$ m/s, respectively). At low gas flow rate ratios β, the effect of the bubble size on the gas velocity is insignificant. In the near-wall zone, the velocity profiles for the two-phase flow are more filled compared to the liquid phase velocity; on the contrary, in the near-axis part of the flow these profiles are less filled. Some difference between the velocities of the two phases is observed, which becomes more pronounced as the bubble size increases. It can also be noted that the downward bubbly flow displays an increased gradient of liquid-phase velocity in the near-wall zone.

The profiles of the axial liquid-phase velocity for various values of β are shown in Fig. 4. Both measured and predicted profiles of the gas–liquid flow velocity become more filled with increasing β. Even low concentrations of bubbles ($\beta = 2\%$) result in a strong deformation of the liquid velocity compared to the case of single-phase flow. As the volumetric gas flow rate increases, the gradient of the average carrier-phase velocity in the near-wall zone increases. At the maximum volumetric gas flow rate ratios ($\beta = 10\%$), in the near-wall zone there emerge local maxima of liquid velocity. The calculated position of the maximum liquid-

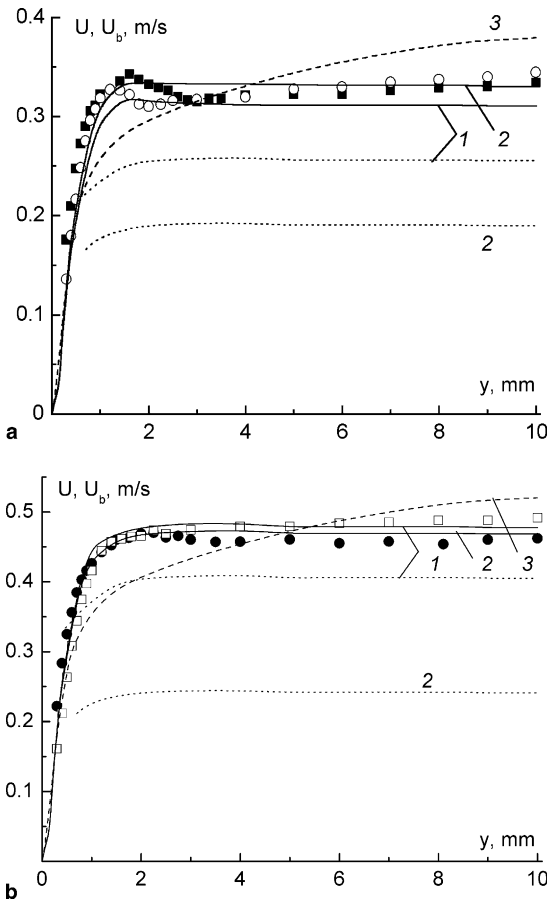

Fig. 3. Profiles of the longitudinal velocities of the phases over the pipe radius. Points—experimental data, curves—predicted data. Solid curves—liquid, dashed curves—gas. (1) $d = 0.613$–0.726 mm, (2) 1.62–1.76 mm, (3) $\beta = 0$, (a) $U_1 = 0.3$ m/s, (b) 0.4 m/s.

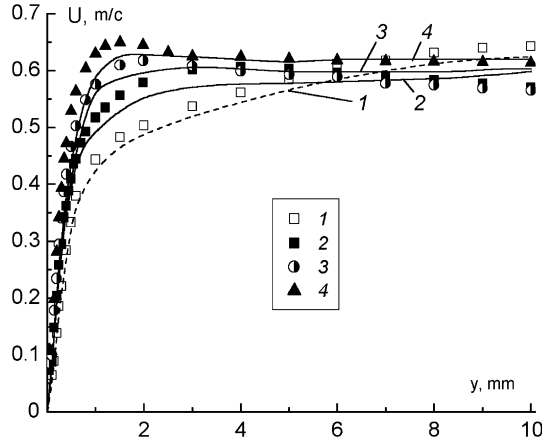

Fig. 4. Effect of the inlet gas flow ratio on the axial velocity of the liquid phase. (1) $\beta = 0$, (2) 0.02, (3) 0.05, (4) 0.1. $U_1 = 0.5$ m/s, $d = 1.7$ mm. Solid curves—liquid in two-phase flow, dashed curve—one-phase liquid flow.

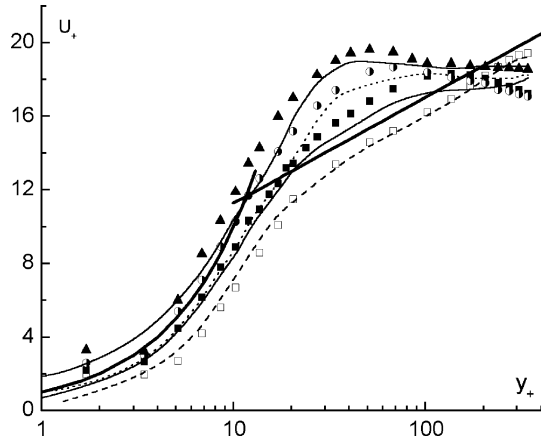

Fig. 5. Profiles of liquid velocity in the universal coordinates. The designations are the same as in Fig. 4.

phase velocity closely agrees with the measured value (within 10%).

The profiles of liquid-phase velocity plotted in the universal coordinates are shown in Fig. 5. An analysis of the data shows that for the single-phase water flow a good agreement is observed between the measured and predicted velocities of the liquid phase. Note that the variation of the inlet gas flow rate ratio in the range $\beta = 1$–10% results in no substantial changes of the liquid-phase velocity in the viscous sublayer compared to the logarithmic profile. In the first-order approximation, at low gas flow rate ratios the velocity profiles can be predicted as the classical distribution for laminar sublayer. A largest deformation of velocity profiles is observed in the buffer layer, this observation being consistent with the data in Fig. 5. In the near-axis zone of the two-phase flow, the velocity profiles of the continuous phase somewhat overly the logarithmic profile and the velocity profile for the single-phase water flow.

7.2. Fluctuating velocities of the phases

Distributions of axial velocity fluctuations of liquid ($\langle u^2\rangle/U$) and bubbles ($\langle u_b^2\rangle/U$) are shown in Fig. 6a and b ($U_1 = 0.3$ and $U_1 = 0.4$ m/s, respectively). Here, U is the local averaged velocity of the liquid phase. Near the pipe wall, the longitudinal fluctuations of the liquid velocity in the two-phase flow are weaker than in the single-phase flow because the liquid here undergoes mixing under the action of gas bubbles that move with non-zero relative velocity with respect to the water. An increase in the bubble size enhances the turbulence of the two-phase gas–liquid flow. This fact can be explained by flow turbulization caused by the liquid-flow separation on large particles. The bubble velocity fluctuation $\langle u_b\rangle/U$ are weaker than the corresponding liquid-velocity fluctuations; this fact can be explained by the involvement of large bubbles in the turbulent motion of the liquid phase.

Distributions of the axial velocity fluctuations of liquid versus the void fraction of the flow are shown in Fig. 7. Near the wall, the values of $\langle u^2\rangle/U$ are lower than in the

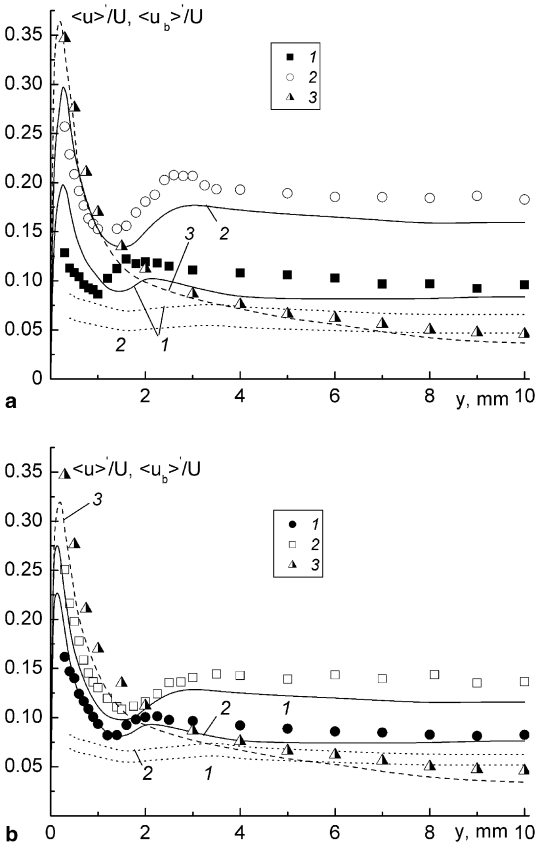

Fig. 6. Axial fluctuations of the phases in the gas–liquid flow. (a) $U_1 = 0.3$ m/s, (b) 0.4 m/s. (1) $d = 0.613$ mm, (2) 1.62 mm, (3) one-phase liquid flow ($d = 0$). Solid curves—liquid in two-phase flow, dashed curves—gas in two-phase flow, dotted curve—one-phase liquid flow.

case of the single-phase flow. The pulsations become weaker in the flow region where the void fraction α almost vanishes.

7.3. Distribution of local void fraction

Fig. 8 illustrates the effect of bubble sizes on the profiles of the local void fraction α at fixed volumetric gas flow rate ratios β (a—across the pipe, b—near-wall part). An increase in the dispersed-phase size is seen to appreciably affect the profiles of α. Finer bubbles approach the wall more closely; this finding can be attributed to lower values of the radial force factors such as the lift force, the turbulent migration force, and the wall force. The latter is seen from the predicted concentration profiles in the near-wall zone (see Fig. 8b) and complies with the measurement data of [6,7].

The predicted and measured profiles of the local void fraction across the channel for various inlet volumetric gas flow rate ratios are shown in Fig. 9. The measured and simulated data indicate that in downward bubbly flows the air bubbles are accumulated in the flow core. In the major portion of the channel the distribution of the local void fraction is roughly uniform across the pipe. At the highest gas flow rate ratios ($\beta = 10\%$), the experimental

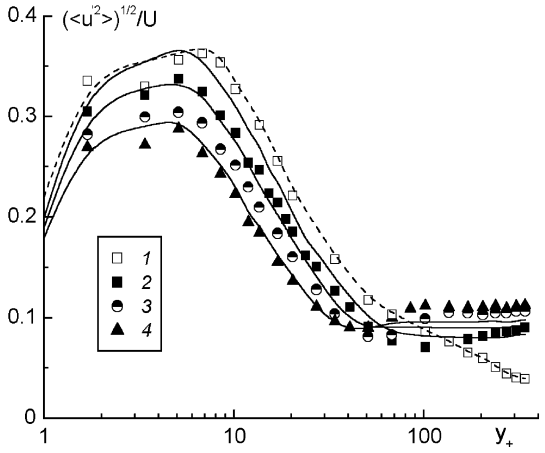

Fig. 7. Root-mean-square pulsations of liquid velocity. The designations are the same as in Fig. 4.

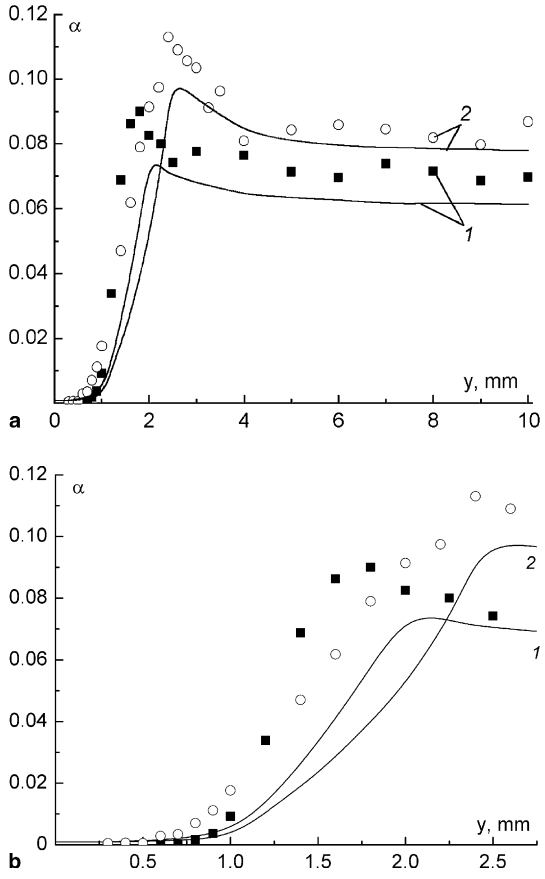

Fig. 8. Local gas void fraction profiles for various bubble sizes. (a) Across the flow, (b) in the near-wall zone. (1) $d = 0.613$–0.726 mm, (2) 1.62–1.76 mm, $U_1 = 0.3$ m/s, $\beta = 0.05$.

data exhibit a maximum in the profiles of α. In the predicted data, the maximum is lower in amplitude, shifted towards the pipe axis. The experimental profiles of α feature almost zero void fraction near the pipe wall; in the predicted data, an appreciable decrease in the amount of bubbles in the near-wall zone is also observed, but here $\alpha > 0$, especially in the case of the maximum void fraction

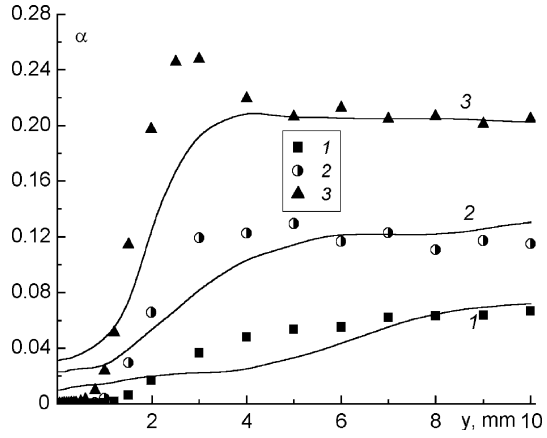

Fig. 9. Effect of the volumetric gas flow ratio on the void fraction. (1) $\beta = 0.02$, (2) 0.05, (3) 0.1. $U_1 = 0.5$ m/s, $d = 1.75$ mm.

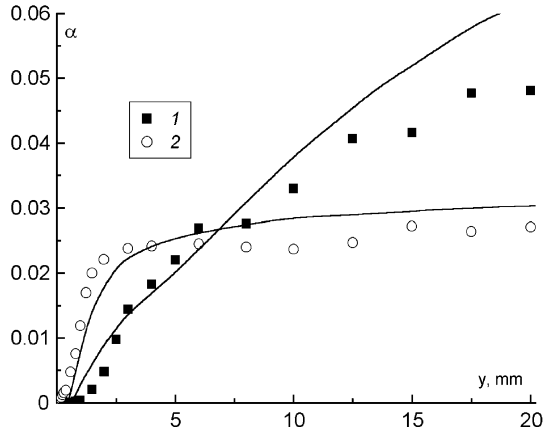

Fig. 10. Effect of the bubble size on the void fraction. Points—experimental data of [7], curves—predicted data. $U_1 = 1$ m/s, $\beta = 0.02$, $2R = 42.2$ mm, $x/(2R) = 100$. (1) $d = 1.5$ mm, (2) 0.8 mm.

($\alpha \approx 0.03$). The thickness of the near-wall layer free of bubbles depends on β. As the inlet volumetric gas flow rate ratio increases, the zone free of bubbles becomes narrower.

Fig. 10 shows the experimental and predicted data [6] for various mean bubble sizes obtained for a pipe with the diameter $2R = 42.2$ mm. The superficial liquid velocity here is $U_1 = 1$ m/s, the pipe Reynolds number is $Re = 43{,}500$, and the gas flow rate ratio is $\beta = 2\%$. An increase in the dispersed-phase size enhances the transverse migration of bubbles; as a result, the near-wall zone free of bubbles becomes narrower, and the local concentration maximum in the near-axis zone, more distinct. Finer bubbles approach the wall more closely. The latter can be explained by weaker effect of the Saffman and turbulent migration forces on the radial migration of fine bubbles.

7.4. Distribution of forces acting on a bubble in the turbulent flow

Fig. 11 shows the distributions of radial forces acting on bubbles in downward gas–liquid flows versus the size of gas

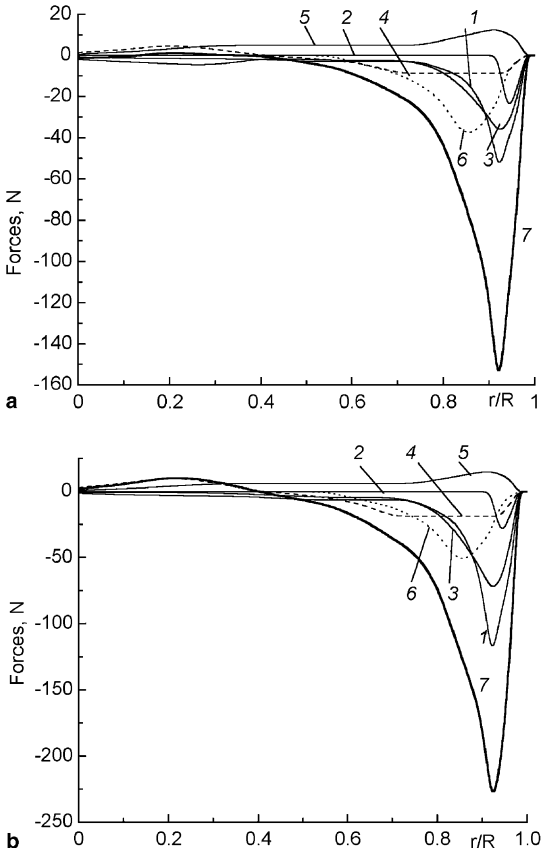

Fig. 11. Distribution of the force factors over the pipe radius. (a) $d = 0.726$ mm, (b) 1.76 mm. (1) Lift force; (2) wall force; (3) turbulent migration (turbophoresis force); (4) drag force; (5) turbulent diffusion; (6) turbulent dispersion; (7) total.

inclusions (the bubble size here is 0.726 mm and 1.76 mm for Fig. 11a and b, respectively). The positive direction is the direction from the pipe axis towards the wall. An analysis of the calculation data in Fig. 11 allows the following conclusions to be drawn. As the bubble size increases, the forces acting on the dispersed phase substantially increase in value. The majority of the force factors retain negative sign over the whole cross-section of the pipe. The largest absolute values are displayed by the lifting force, the turbulent-migration force, and the turbulent-dispersion force. The maxima of these forces are located in the immediate vicinity of the wall. Towards the pipe axis, these forces reduce markedly. All the other forces considered in the present study (namely, the wall force, the drag, and the turbulent-diffusion force) are appreciably weaker. The data of Fig. 11 prove that the major forces causing the transverse migration in downward flows are the lift (Saffman) force, the turbulent migration (turbophoresis) force, and the turbulent dispersion force.

7.5. Wall shear stress

The predicted and measured wall shear stresses [6] versus the Reynolds number are shown in Fig. 12. With increase in the flow velocity, an increase of τ_W is observed.

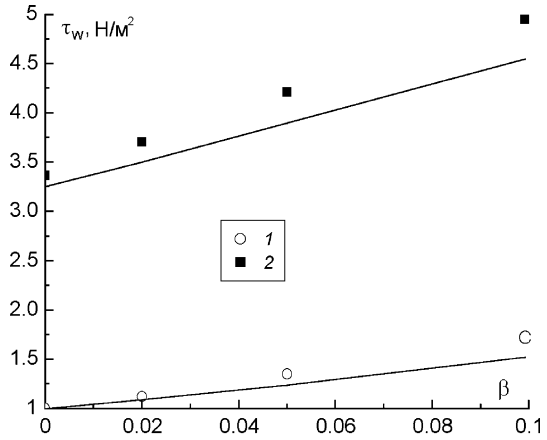

Fig. 12. Friction profiles versus the bubble concentration. Points—experimental data of [7], curves—predicted data, (1) $Re = 10{,}310$, (2) 20,620.

As the volumetric gas flow rate β increases, the wall friction also increases. This regularity can be traced both in the experimental and predicted datasets. An almost linear dependence of wall shear stress versus the inlet gas flow rate ratio is observed. One of the reasons for the increased wall friction is the increase in the liquid velocity gradient in the near-wall zone at the expense of more gently sloping velocity profile in the flow core.

8. Conclusions

An Eulerian two-fluid model was developed to predict momentum- and mass-transfer processes in two-phase downward gas–liquid channel flow. To model the liquid-phase turbulence, the modified k–$\tilde{\varepsilon}$ model of turbulence is used. For the dispersed phase, relations of [34] were used, which were initially developed for the solid phase and then successfully applied to gas-drop flows with droplet evaporation.

A numerical simulation of the downward bubbly flow in a pipe and a comparison with experimental data are performed. Even low concentrations of bubbles cause a substantial deformation of liquid-velocity profiles compared to the single-phase flow, especially, in the near-wall zone. As the gas flow rate ratio at the inlet to the pipe increases, local maxima of the carrier phase velocity emerge in the near-wall zone. The model satisfactorily predicts the velocities of the two phases in the two-phase flow. In the vicinity of the wall, the liquid-velocity pulsations are weaker compared to those in the single-phase flow. In the near-axis zone, the pulsations are more intense than in the single-phase flow. The model is shown to be capable of qualitative prediction of cross-sectional distributions of bubbles across the pipe. A good agreement is observed between the predicted data and measured averaged velocities of liquid, pulsations of this velocity, and cross-sectional void fraction profiles.

The distribution of the forces acting on a bubble in downward gas–liquid flow was revealed. It is shown that,

as the bubble size increases, the forces acting on the dispersed phase become stronger. Most forces are negative throughout the whole cross-section of the flow. Largest absolute values are displayed by the lifting force, the turbulent-migration force, and the turbulent-dispersion force. The maxima of the forces are observed in the immediate vicinity of the pipe wall. The major forces causing the transverse migration in downward flow are the lift (Saffman) force, the turbulent migration (turbophoresis) force, and the turbulent dispersion force.

Acknowledgements

This work was supported in part by the Russian Federation's Presidential Foundation (Grants NSh-1308.2003.8 and MK-1184.2005.8) and by the Russian Foundation for Basic Research (Projects Nos. 04-01-00328, 05-02-16281, 05-08-33586). M. Pakhomov thanks Russian Science Support Foundation for their grant for Young PhD Scientist-2005.

References

[1] T. Oshinovo, M.E. Charles, Vertical two-phase flow, Part II. Holdup and pressure drop, Can. J. Chem. Eng. 52 (1974) 438–448.
[2] B.G. Ganchev, V.G. Peresad'ko, Hydrodynamics and heat transfer processes in descending bubble flows, J. Eng. Phys. 49 (1985) 181–189.
[3] R.S. Gorelik, O.N. Kashinsky, V.E. Nakoryakov, Study of downward bubbly flow in a vertical pipe, J. Appl. Mech. Techn. Phys. (1) (1987) 69–73.
[4] S.K. Wang, S.J. Lee, O.S. Jones Jr., R.T. Lahey Jr., 3-D turbulence structure and phase distribution measurements in bubbly two-phase flows, Int. J. Multiphase Flow 13 (1987) 327–343.
[5] K. Usui, K. Sato, Vertically downward two-phase flow: Part 1. Void distribution and average void fraction, J. Nucl. Sci. Technol. 26 (1989) 670–680.
[6] O.N. Kashinsky, V.V. Randin, Downward bubble gas–liquid flow in a vertical pipe, Thermophys. Aeromech. 6 (2) (1999) 221–229.
[7] O.N. Kashinsky, V.V. Randin, Downward bubble gas–liquid flow in a vertical pipe, Int. J. Multiphase Flow 25 (1999) 109–138.
[8] T. Hibiki, H. Goda, S. Kim, M. Ishii, J. Uhle, Experimental study on interfacial area transport of a vertical downward bubbly flow, Exp. Fluids 35 (2003) 100–111.
[9] T. Hibiki, H. Goda, S. Kim, M. Ishii, J. Uhle, Structure of vertical downward bubbly flow, Int. J. Heat Mass Transfer 47 (2004) 1847–1862.
[10] X. Sun, S. Paranjare, M. Ishii, J. Uhle, LDA measurement in air–water downward flow, Int. J. Exp. Therm. Fluid Sci. 28 (2004) 317–328.
[11] X. Sun, S. Paranjare, S. Kim, B. Ozar, M. Ishii, Liquid velocity in upward and downward air–water flows, Ann. Nucl. Energy 31 (2004) 357–373.
[12] O.N. Kashinsky, V.V. Randin, P.D. Lobanov, T.D. Chimitov, Bubbly downflow at a low void fraction, Thermophys. Aeromech. 11 (4) (2004) 603–608.
[13] V.K. Artemiev, Yu.N. Kornienko, Numerical modeling of influence non-monotonic profile of gas (vapor) content on a distribution of velocity and temperature in a two-phase bubbly flow, in: Proceedings of 3rd Russian National Conference on Heat Transfer, vol. 5, Moscow, Russia, 21–25 October 2002, pp. 41–44 (in Russian).
[14] J. Chahed, V. Roig, L. Masbernat, Eulerian–Eulerian two-fluid model for turbulent gas–liquid bubbly flows, Int. J. Multiphase Flow 29 (2003) 23–49.
[15] L.I. Zaichik, A.P. Skibin, S.L. Soloviev, Simulation of the distribution of bubbles in a turbulent liquid using a diffusion-inertia model, High Temp. 42 (2004) 111–118.
[16] A. Kamp, C. Colin, J. Fabre, The local structure of a turbulent bubble pipe flow under different gravity conditions, in: Proceedings of 2nd International Conference on Multiphase Flow ICMF-95, Kyoto, Japan, vol. 3, 1995, Paper No. P6.
[17] S.L. Lee, R.T. Lahey Jr., O.C. Jones, The prediction of two-phase turbulence and phase distribution phenomena using a k–ε model, Jpn. J. Multiphase Flow 3 (1989) 335–368.
[18] S.P. Antal, R.T. Lahey Jr., J.F. Flaherty, Analysis of phase distribution in fully developed laminar bubbly of two-phase flow, Int. J. Multiphase Flow 17 (1991) 363–652.
[19] M.A. Lopez de Bertodano, R.T. Lahey Jr., O.C. Jones, Phase distribution in bubbly two-phase flow in vertical ducts, Int. J. Multiphase Flow 20 (1994) 805–818.
[20] A. Tomiyama, Struggle with computational bubble dynamics, in: Proceedings of 3rd International Conference on Multiphase Flow ICMF-98, Lyon, France, June 8–12, 1998, CD-ROM, Paper No. 004.
[21] P.M. Carrica, D.A. Drew, F. Bonetto, R.T. Lahey Jr., A polydisperse model for bubbly two-phase flow around surface ship, Int. J. Multiphase Flow 25 (1999) 257–305.
[22] A.A. Troshko, Y.A. Hassan, A two-equation turbulence model of turbulent bubbly flow, Int. J. Multiphase Flow 27 (2001) 1965–2000.
[23] M.S. Politano, P.M. Carrica, J. Converti, A model for turbulent polydisperse two-phase flow in vertical channel, Int. J. Multiphase Flow 29 (2003) 1153–1182.
[24] H. Goda, T. Hibiki, S. Kim, M. Ishii, J. Uhle, Drift-flux model for downward two-phase flow, Int. J. Heat Mass Transfer 46 (2003) 4835–4844.
[25] N. Zuber, J.A. Findlay, Average volumetric concentration in two-phase flow systems, ASME J. Heat Transfer 87 (1965) 453–468.
[26] V.E. Nakoryakov, O.N. Kashinsky, A.P. Burdukov, V.P. Odnoral, Local characteristics of upward gas–liquid flows, Int. J. Multiphase Flow 7 (1981) 63–81.
[27] V.E. Nakoryakov, O.N. Kashinsky, V.V. Randin, L.S. Timkin, Gas–liquid bubbly flow in vertical pipes, ASME J. Fluids Eng. 118 (1996) 377–382.
[28] V.I. Terekhov, M.A. Pakhomov, The numerical modeling of the tube turbulent gas-drop flow with phase changes, Int. J. Therm. Sci. 43 (2004) 595–610.
[29] V.I. Terekhov, M.A. Pakhomov, The thermal efficiency of near-wall gas-droplets screens, Part I. Numerical modeling, Int. J. Heat Mass Transfer 48 (2005) 1747–1759.
[30] D.A. Drew, Mathematical modeling of two-phase flow, Ann. Rev. Fluid Mech. 15 (1983) 261–291.
[31] R.I. Nigmatulin, Dynamics of Multiphase Media, Hemisphere, Washington, 1991.
[32] C.T. Crowe, M. Sommerfeld, Y. Tsuji, Multiphase Flow with Droplets and Particles, CRC, Boca Raton, Florida, USA, 1998.
[33] T.R. Auton, J.C.R. Hunt, M. Prud'homme, The force exerted on a body in inviscid unsteady non-uniform rotational flow, J. Fluid Mech. 197 (1988) 241–257.
[34] I.V. Derevich, The hydrodynamics and heat transfer and mass transfer of particles under conditions of turbulent flow of gas suspension in a pipe and in an axisymmetric jet, High Temp. 40 (2002) 78–91.
[35] C.B. Hwang, C.A. Lin, Improved low-Reynolds-number k–$\tilde{\varepsilon}$ model based on direct simulation data, AIAA J. 36 (1998) 38–43.
[36] K.-C. Chang, M.-J. Shyu, Revisiting the Reynolds-averaged energy equation in near-wall turbulence model, Int. J. Heat Mass Transfer 43 (2000) 665–676.
[37] I.Yu. Brailovskaya, L.A. Chudov, The solution of boundary layer equations with finite-difference method, Comput. Meth. Program. (1962) 167–182 (in Russian).
[38] C.A.J. FletcherComputational Techniques for Fluid Dynamics, vol. 2, Springer-Verlag, Berlin, 1988.